Electronic Supporting Information

Comparative study of sonication-assisted liquid phase exfoliation of six layered coordination polymers

By Jonas Gosch, [a‡] Kevin Synnatschke, [b‡] Norbert Stock *[a] and Claudia Backes *[c]

[a]Christian-Albrechts-Universität zu Kiel, 24118 Kiel, Max-Eyth-Straße 2.
[b]University of Dublin, Trinity College, Dublin 2, SNIAM Building.
[c]University of Kassel, D-34132 Kassel, Heinrich-Plett-Str. 40.
[‡]*both authors contributed equally.*

Content

1. Experimental section

1.1 Materials and methods

All chemicals were purchased commercially and used without further purification. Gallium nitrate hydrate ($Ga(NO_3)_3 \cdot 7H_2O$, abcr, 99.99% puratrem), naphthalene-1,8-dicarboxylic anhydride (TCI, >98%), zirconium(IV)-chloride (abcr, 99,95%), 4,4'-oxybis(benzoic acid) (TCI, >98%), N,N'-dimethylformamide (Grüssing, 99%), formic acid (BASF, 98%), scandium nitrate pentahydrate ($Sc(NO_3)_3 \cdot 5H_2O$, abcr, 99.9%), 2,2'-bipyridine-5,5'-dicarboxylic acid (abcr, 97%), 4,4'-sulfonyldibenzoic acid (sigma aldrich, 98%), 5-aminoisophthalic acid (abcr, 95%), acetic anhydride (Grüssing, 99%), acetic acid (VWR chemicals, Glacial), zirconium acetate solution in dilute acetic acid (sigma aldrich, 15-17 wt% Zr), dichloromethane (VWR chemicals, 99.5%), zirconium oxychloride octahydrate ($ZrOCl_2 \cdot 8H_2O$, abcr, 98%), Ethanol (Walter CMP, 99%), 5 nitropicolinic acid (abcr, 98%), sodium hydroxide (Grüssing, 99%), D-glucose (Grüssing), hydrochloric acid (VWR, 37%), sodium cholate hydrate (sigma aldrich, ≥97).

Microwave-assisted syntheses were performed with a Biotage Initiator Classic microwave oven.

Scanning electron microscopy (SEM) images were acquired with a JEOL JSM-7610F field emission scanning electron microscope (FE-SEM), using an In-lens Schottky field emission electron gun with 1-2 kV acceleration voltage at 2.5×10^{-9} mbar. The images were measured with a dual (upper and lower) detector system consisting of collector-, scintillator-, light guide- and photomultiplier units for secondary electron imaging (SEI).

Powder X-ray diffraction (PXRD) data was collected on a Stoe Stadi MP diffractometer equipped with a MYTHEN 1 K detector ($CuK_{\alpha 1}$-radiation, λ = 1.5406 Å).

IR spectra were recorded at room temperature on a Bruker Vertex70 FT-IR spectrometer using a broadband spectral range extension VERTEX FM for full mid and far IR in the range of 6.000-80 cm^{-1}.

Raman spectra for the initial characterization were recorded at RT on a Bruker RAM II FT-Raman spectrometer using a liquid nitrogen cooled, highly sensitive Ge detector, 1064 nm radiation and 4 cm^{-1} resolution (300 scans, focal length 100 mm, laser power 100 mW). The Raman measurements of the exfoliated species were acquired using a Renishaw InVia-Reflex confocal Raman microscope with a 532 nm excitation laser in air under ambient conditions. The spectra of the nanomaterial were acquired after drop casting nanomaterial onto a gold-coated aluminum substrate. Spectra were acquired by averaging 5000 accumulations at two different spots to account for low signal to noise ratios. The Raman emission was collected through a 50x, long working distance objective lens in streamline mode and dispersed by a 2400 l/mm grating with 0.5% of the laser power (<0.1 mW). Note that the laser power has to be kept as low as possible to avoid heating and sample decomposition. Typical acquisition times were 24 h per spectrum.

Atomic force microscopy was performed on a Dimension ICON3 scanning probe microscope (Bruker AXS S.A.S.) in ScanAsyst mode in air under ambient conditions using aluminium coated silicon cantilevers (OLTESP-R3). The concentrated dispersions were diluted with water to optical densities <0.1 across the resonant spectral region. A drop of the dilute dispersions (20 µL) was deposited on a pre-heated (180°C) Si/SiO_2 wafers (0.5x0.5 cm^2) with an oxide layer of 300 nm. After deposition, the wafers were rinsed with ~5 mL of water and ~5 mL of isopropanol. Typical image sizes ranged from 30x30 μm^2 for larger- to 10x10 μm^2 for smaller nanosheets at scan rates of 0.5-0.8 Hz with 1024 lines per image. Previously published length corrections were used to correct lateral dimensions from cantilever broadening and pixilation effects.[1]

1.2 Detailed synthesis procedures for Ga-1,8-ndc, ScBPyDC, Sc-CAU-11, Zr-FA-ODB, Zr-CAU-39 and Zr-CAU-45.

Table S1: Summarized synthesis parameters of all CPs under study.

compound	metal salt	solvent	modulator	heating	T, t / °C, min
Ga-1,8-ndc	$Ga(NO_3)_3 \cdot x\ H_2O$	water	NaOH	microwave	140, 240
Sc-BPyDC	$Sc(NO_3)_3 \cdot 5\ H_2O$	DMF	HCl	conv.	160, 120
Sc-CAU-11	$Sc(NO_3)_3 \cdot 5\ H_2O$	water/DMF	-	microwave	160, 120
Zr-FA-ODB	$ZrCl_4$	DMF	formic acid	conv.	120, 2880
Zr-CAU-39	$ZrOCl_2 \cdot 8\ H_2O$	water	formic acid	conv.	140, 40
Zr-CAU-45	$Zr(CH_3COO)_4$-sol.	acetic acid	-	conv.	160, 1320

Synthesis of Ga-1,8-ndc

[Ga(OH)(1,8-ndc)], 1,8-ndc^{2-} = 1,8-naphthalene dicarboxylate ($C_{12}H_6O_4$), was synthesized according to literature.[2] The reaction was carried out under hydrothermal conditions in 20 mL glass vials using microwave-assisted heating. Therefore, 99 mg (5 mmol) of naphthalene-1,8-dicarboxylic anhydride was employed to the glass reactor and 0.5 mL gallium nitrate solution (0.72 mol/l) (3.6 mmol), 0.5 mL NaOH solution (2 mol/l) (1 mmol) and 9 mL of water were added. The reactor was sealed and heated at 140 °C for 4 h under stirring. The product was centrifuged off, washed twice with DMF and ethanol respectively and dried at 85 °C for 16 h. Ga-1,8-ndc was obtained as a colorless microcrystalline powder.

Synthesis of ScBPyDC

[Sc(OH)(BPyDC)] was synthesized according to literature.[3] The reaction was carried out under hydrothermal conditions in 2 mL Teflon reactors using conventional heating. Therefore, 2,2′-bipyridine-5,5′-dicarboxylic acid (H_2BPyDC, $C_{12}H_8N_2O_4$) (7.6 mg, 0.031 mmol) and $Sc(NO_3)_3 \cdot 5H2O$ (20.1 mg, 0.062 mmol) were employed in the reactor and 1 mL DMF as well as 200 µL HCl (2 M in water) were added. The reactor was heated to 160 °C within 2 h. The temperature was kept for 48 h and cooled down to ambient temperature within 6 h. The product was filtered off and washed thoroughly with deionized water before being dried at air. Sc-BPyDC was obtained as a beige microcrystalline powder.

Synthesis of Sc-CAU-11

[Sc(OH)(SDBA)] was synthesized according to literature.[4] The reaction was carried out under hydrothermal conditions in 2 mL glass reactors using microwave-assisted heating. Therefore, 19.2 mg (62.6 µmol) 4,4-sulfonyldibenzoic acid (H_2SDBA, $C_{14}H_{10}O_6S$) and 20.0 mg (62.6 µmol) $Sc(NO_3)_3 \cdot 5H_2O$ were employed to the reactor and 0.4 mL of water and 1.6 mL DMF were added. The reactor was sealed and heated at 160 °C for 2 h. The precipitate was filtered off, washed twice with water and dried in air. Sc-CAU-11 was obtained as a colorless microcrystalline powder.

Synthesis of Zr-FA-ODB

$[Zr_6O_4(OH)_4(HCOO)_{12}] \cdot H_2ODB \cdot 1.5HCl \cdot 0.7DMF$ was synthesized in 2 mL Teflon reactors using conventional heating. Therefore, 36.1 mg (155 µmol) $ZrCl_4$ were employed to the reactor and a solution of 4,4′-Oxybis(benzoic acid) (H_2ODB, $C_{14}H_{10}O_5$) in DMF (0.4 mL, 0.1936 M, 77.5 µmol) as well as

0.614 mL of formic acid and 0.586 mL DMF were added. The reactor was sealed, heated to 120 °C within 1 h and the temperature was kept for 48 h. After slowly cooling down to ambient temperature for 12 h, the precipitate was filtered off, washed twice with DMF and acetone respectively and dried at air. Zr-ODB was obtained as a colorless microcrystalline powder.

Synthesis of Zr-CAU-39

$[Zr_{12}O_8(OH)_8(OH)_6(OH)_6(H_2O)_6(APDC)_6]$ was synthesized according to literature.[5] The reaction was carried out under hydrothermal conditions in 7 mL Pyrex tubes using conventional heating. Therefore, 16.1 mg (50 µmol) $ZrOCl_2 \cdot 8H_2O$ and 13.6 mg (50 µmol) azopyridinedicarboxylic acid (H_2APDC, $C_{12}H_8N_4O_4$) were employed to the reactor and 1.2 mL of water and 0.8 mL acetic acid were added. The Pyrex tube was sealed, placed in an aluminum heating block and heated at 140 °C for 40 min under stirring. The product was isolated by filtration, washed twice with water and ethanol respectively and dried at air. Ce-CAU-39 was obtained as an orange microcrystalline powder.

Synthesis of Zr-CAU-45

$[Zr_{30}O_{20}(OH)_{26}(OAc)_{18}L_{18}]$ was synthesized according to literature.[6] The reaction was carried out under hydrothermal conditions in a 20 mL PTFE lined steel autoclave using conventional heating. Therefore, 446.4 mg (2.00 mmol) 5-acetamidoisophthalic acid (H_2L, $C_{10}H_9NO_5$) and 17 mL acetic acid were employed and 0.892 mL (2.13 mmol) zirconium acetate solution in dilute acetic acid were added. The autoclave was sealed and heated to 160 °C within one hour. After keeping the temperature for 22 hours, the reaction mixture was slowly cooled to ambient temperature over 24 h. The precipitate was filtered off and dried at 50°C for 4h. Purification of CAU-45 was accomplished by stirring the crude powder for 2 h in DMF at room temperature. In order to exchange the solvent, the powder was isolated by filtration, washed with 200 mL of dichloromethane and redispersed in 20 mL of dichloromethane. After stirring for 24 h at room temperature, CAU-45 was collected as a pale ocher microcrystalline powder.

1.3 Crystal structure of Zr-FA-ODB

The coordination polymer Zr-FA-ODB crystallizes in the monoclinic spacegroup *C2/m*. The crystal structure was determined from X-ray powder diffraction data using the Rietveld refinement method. Lattice parameters and refinement factors are summarized in Table S2. The crystal structure is built up by hexanuclear $[Zr_6O_4(OH)_4]$ clusters and formate ions as bridging linkers (Figure S1). The inorganic building unit is well known from other porous CPs[7] and consists of six octahedrally arranged Zr^{4+} ions, each eightfold coordinated by oxygen ions in a square antiprismatic fashion. The resulting IBUs are interconnected by eight formate ions horizontally along the *bc* plane to form well defined layers. This type of zirconium formate layers was observed in the literature before.[8] However, the stacking of layers in Zr-FA-ODB differs from the reported structure. The layers formed in this way lie parallel to the *bc* plane. In the structure of Zr-FA-ODB, two of these layers are stacked together in an offset manner to form double layers (Figure S1, left). Stacking of these double layers results in a rather large gap in which the chloride ions and NN'-dimethyl formamide molecules are expected to be located. The position of the 4,4-oxybis(benzoic acid) molecules that were deployed in the synthesis could not be located during the refinement process and are either freely deposited in these gaps or coordinated to the respective sheets.

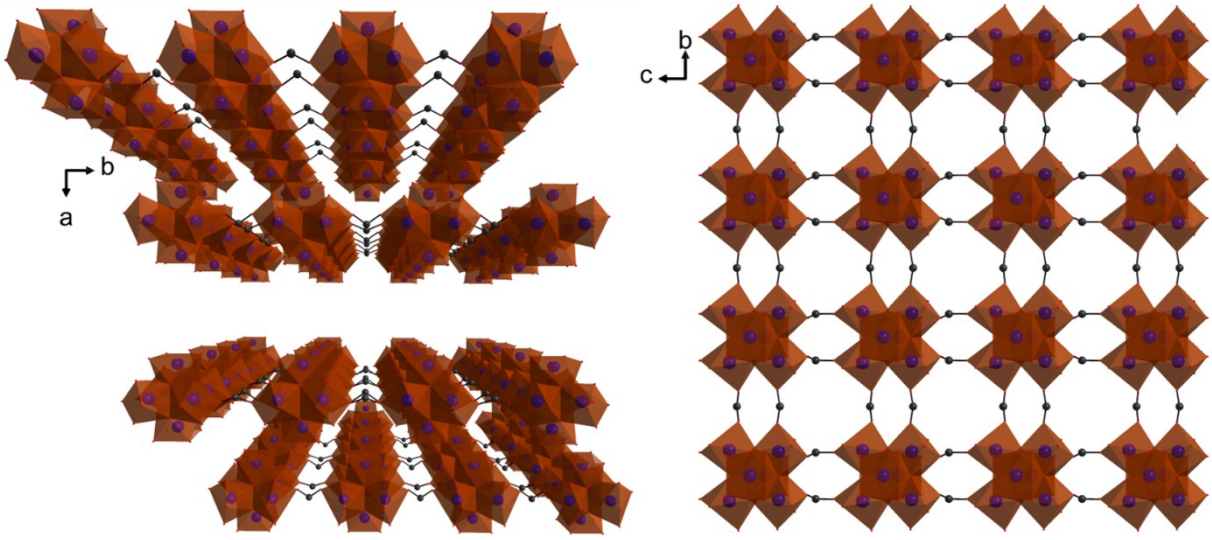

Figure S1: Crystal structure of Zr-FA-ODB from two different perspectives.

Table S2: Lattice parameters and refinement factors of Zr-FA-ODB.

crystal system	**monoclinic**
space group	*C*2/*m*
a	48.803(4) Å
b	9.9808(5) Å
c	9.9592(6) Å
β	105.618(7) °
V	4672.0(6) Å^3
R_{wp}	8.3
GoF	3.97

1.4 Liquid phase exfoliation

Exfoliation of the layered CPs was achieved by the following procedure: 5 mg of the bulk material was subjected to LPE by bath sonication in 5 mL aqueous sodium cholate solution (2 g/L) for 7 h. Periodic cooling of the water bath with ice prevented overheating. After exfoliation, two centrifugation steps were applied to the unrefined product: unexfoliated material was removed from the dispersion by sedimentation at 400 *g* (2 h, 5°C). The resulting supernatant was then centrifuged at 30 k *g* (3 h, 5°C) to precipitate the nanomaterial, while soluble impurities or defective nanosheets remained in the dispersion. Centrifugation was performed in a Hettich Mikro 220R centrifuge equipped with a fixed-angle rotor 1195-A in 1.5 mL Eppendorf centrifuge tubes.

To determine the yield, a larger mass required and therefore exfoliation was performed in a larger batch using 50 mg of bulk material and 50 mL of aqueous sodium cholate solution. The yield of exfoliated nanomaterial for each MOF was determined by filtering a known volume of dispersion onto AlOx membranes (pore size 20 nm) and washing with 500 mL DI water. Prior to weighing, membranes were dried in vacuum at 50°C before and after deposition. As the required time for drying varied for the different materials, samples were considered dry after no further mass change was observed between measurements after drying overnight.

We used relatively long sonication times to avoid a large impact of the exfoliation kinetics which might be different for the different compounds in particular at short sonication times. Note that exfoliation

kinetics in LPE are still not fully understood and only relatively simple models exist[7] so that it is not clear in which way the exfoliation rate is governed by the combination of material, solvent and exfoliation technique. Recent insights in the exfoliation mechanism of graphite at the early stages of exfoliation suggests that the fragmentation of the crystals during sonication will depend on the material.[8] However, a frequently made observation in graphite/graphene exfoliation is that the dispersed concentration scales with the square root of the sonication time and after 5-7 h, the dispersed concentration as function of sonication time begins to plateau.[7, 9, 10] While we have not explicitly checked this for the CPs under study, we note that this type of scaling was (roughly) observed for a range of materials beyond graphene such as MoS_2[11], MoO_3,[12] GaS,[13] and BP.[14] Since prolonged sonication might favour sono-chemistry, we have chosen a sonication time of 7h as a compromise that is frequently used in LPE on other materials.

We have chosen aqueous surfactant solution as a stabilizer, since we found that the CPs do not show any sign of degradation (see section on XRD, IR and Raman spectroscopy). Since common LPE solvents[9, 15] such as N-methyl-2-pyrrolidone (NMP) are toxic and often have high boiling points, aqueous surfactant solutions can be regarded as environmentally friendly alternative.[16] Here we chose sodium cholate which is a steroid acid predominantly found in the bile of mammals. In addition to aspects regarding safety and toxicity, we note that high boiling points of the solvents can cause issues on depositing samples for AFM due to the formation of coffee stains. Last but not least, it was demonstrated for graphene that larger portions of smaller/thinner nanosheets can be obtained in aqueous surfactant solution compared to NMP.[17] While this does not necessarily have to be the case for other material system, it could be another advantage, as dispersions containing smaller/thinner nanosheets are easier to characterize with AFM due to a reduced polydispersity.

2. Scanning electron microscopy

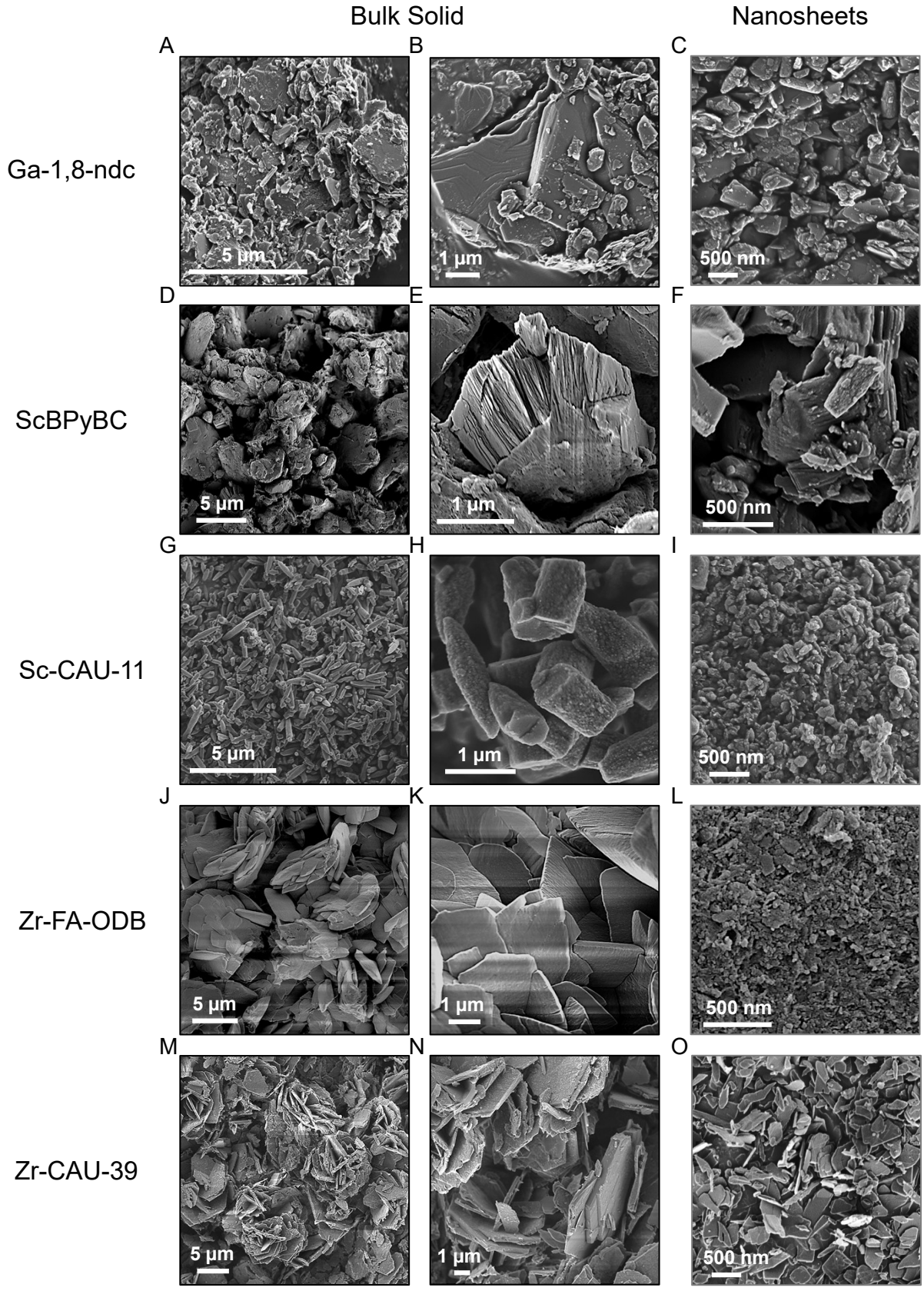

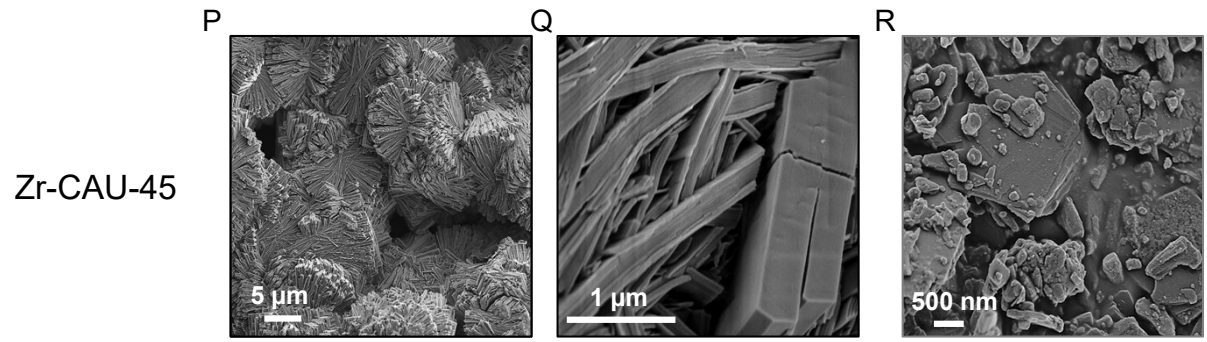

Figure S2: Morphology comparison of the starting materials and the exfoliated nanosheets by SEM. Each row shows images of a different material. The first two columns show representative images of the starting material at different magnification (low resolution: left, high resolution: middle). The third row shows a high resolution image of the corresponding nanomaterial (right). Results are shown for Ga-1,8-ndc (**A-C**), Sc-BPyDC (**D-F**), Sc-CAU-11 (**G-I**), Zr-FA-ODB (**J-L**), Zr-CAU-39 (**M-O**) and Zr-CAU-45 (**P-R**).

3. Diffraction patterns, RAMAN- and IR-spectra

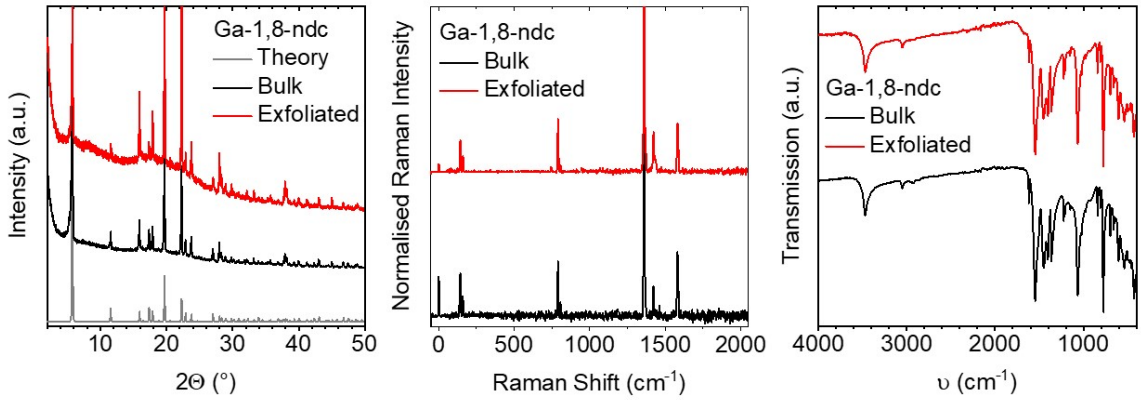

Figure S3: Structural and spectroscopic properties of exfoliated Ga-1,8-ndc (**1**). Acquired diffraction pattern and spectra on the dried nanosheet dispersion are shown in comparison to the bulk sample. (**A**) PXRD data pre and post LPE in comparison to theory. (**B**) Raman and (**C**) IR spectroscopy measurements show no other than the expected signals. The results imply no changes of the material composition and crystallinity upon exfoliation.

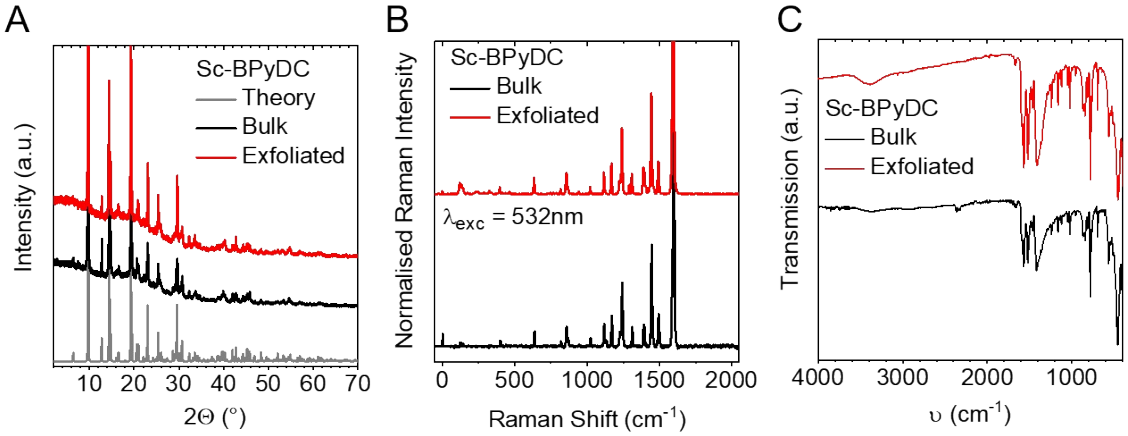

Figure S4: Structural and spectroscopic properties of exfoliated ScBPyDC (**2**). Acquired diffraction pattern and spectra on dried nanosheet dispersions are shown in comparison to the bulk sample. (**A**) PXRD data pre and post LPE in comparison to theory. (**B**) Raman and (**C**) IR spectroscopy measurements show no other than the expected signals. The results imply no changes of the material composition and crystallinity upon exfoliation.

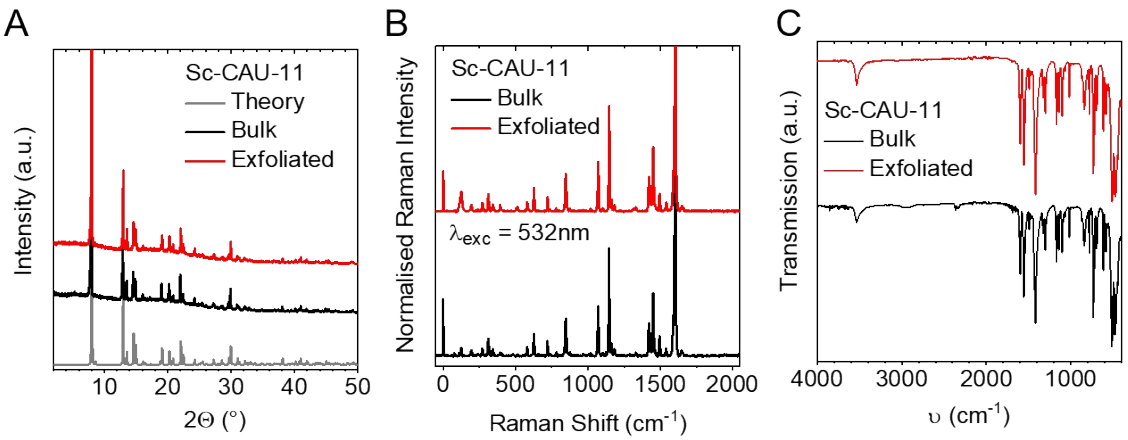

Figure S5: Structural and spectroscopic properties of exfoliated Sc-CAU-11 (**3**). Acquired diffraction pattern and spectra on dried nanosheet dispersion are shown in comparison to the bulk sample. (**A**) PXRD data pre and post LPE in comparison to theory. (**B**) Raman and (**C**) IR spectroscopy measurements show no other than the expected signals. The results imply no changes of the material composition and crystallinity upon exfoliation.

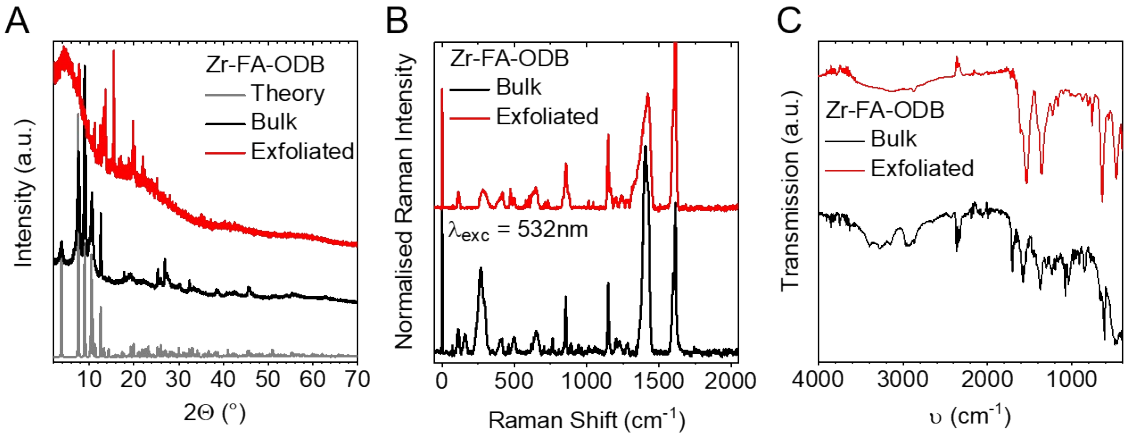

Figure S6: Structural and spectroscopic properties of exfoliated Zr-FA-ODB (**4**). Acquired diffraction pattern and spectra on dried nanosheet dispersion are shown in comparison to the bulk sample. (**A**) PXRD data pre and post LPE in comparison to theory. (**B**) Raman and (**C**) IR spectroscopy measurements reveal great differences between nanosheets and bulk material. The results imply that the exfoliation process leads to significant changes in the structural and spectroscopic properties of the material which we assign to a partial removal of the intercalation layer in the crystal structure.

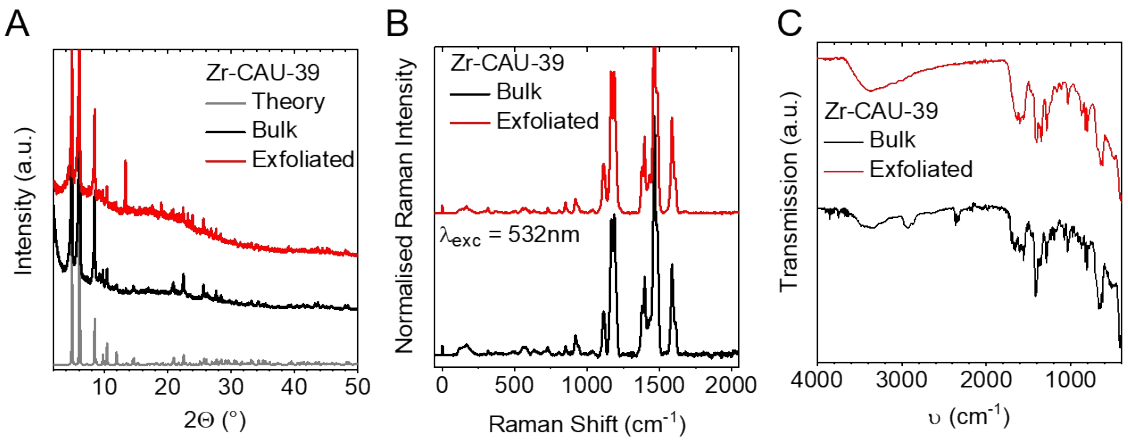

Figure S7: Structural and spectroscopic properties of exfoliated Zr-CAU-39 (**5**). Acquired diffraction pattern and spectra on dried nanosheet dispersion are shown in comparison to the bulk sample. (**A**) PXRD data pre and post LPE in comparison to theory. (**B**) Raman and (**C**) IR spectroscopy measurements show no other than the expected signals. The results imply no changes of the material composition and crystallinity upon exfoliation.

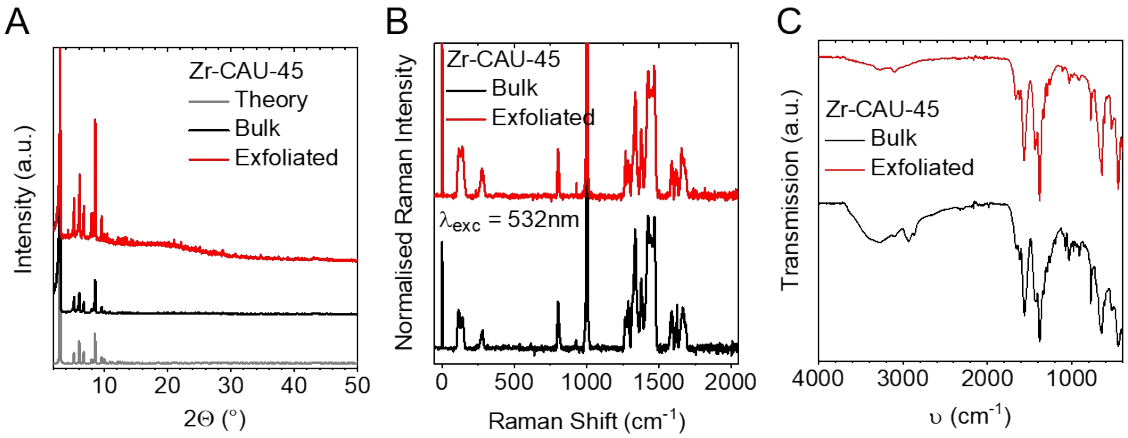

Figure S8: Structural and spectroscopic properties of exfoliated Zr-CAU-45 (**6**). Acquired diffraction pattern and spectra on dried nanosheet dispersion are shown in comparison to the bulk sample. (**A**) PXRD data pre and post LPE in comparison to theory. (**B**) Raman and (**C**) IR spectroscopy measurements show no other than the expected signals. The results imply no changes of the material composition and crystallinity upon exfoliation.

4. Statistical AFM analysis

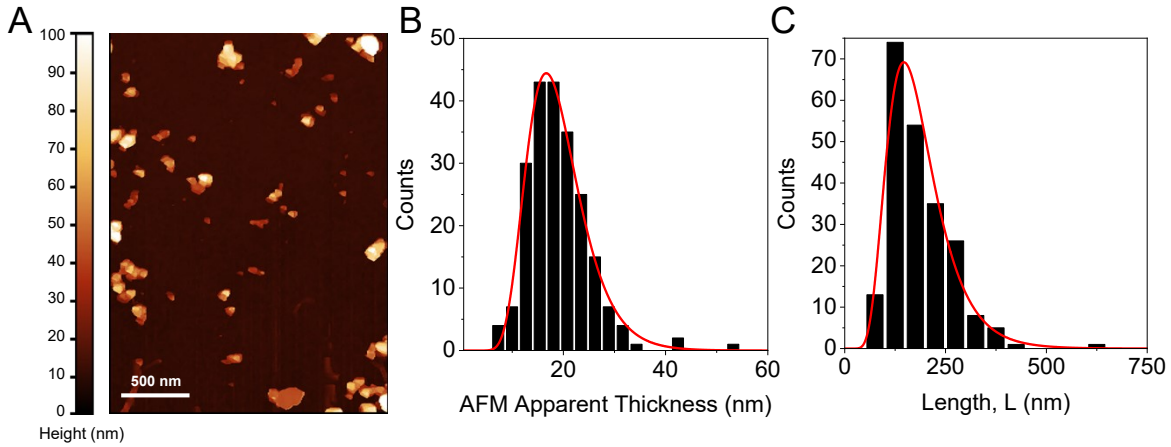

Figure S9: Raw data from the statistical AFM analysis. (**A**) Representative wide-view AFM image of the exfoliated Ga-1,8-ndc (**1**). Thickness (**B**) and length (**C**) distribution histograms of the sample after the exfoliation. An arithmetic mean length, <L> of ~150 nm with an average thickness, <T> of ~19 nm is determined after measuring the dimensions of more than 200 individual nanosheets.

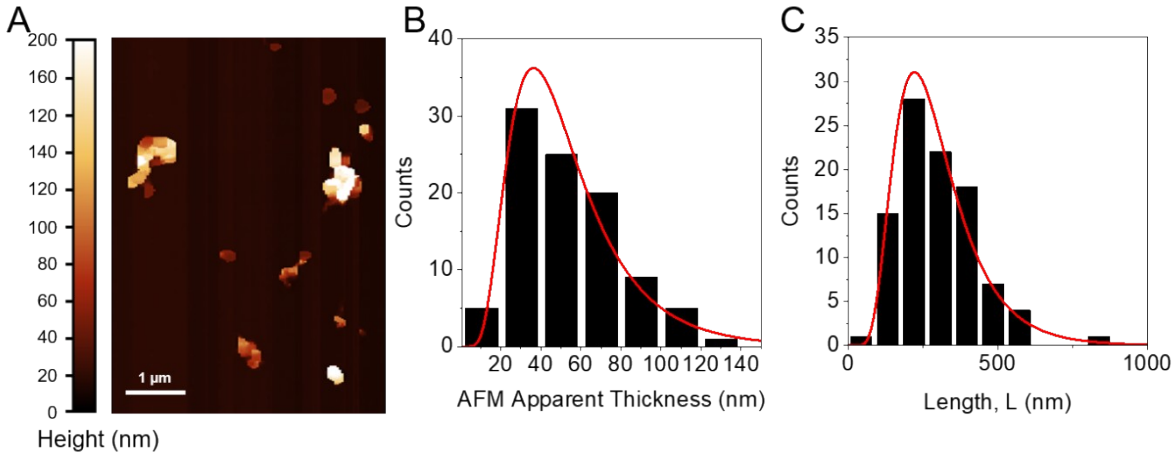

Figure S10: Raw data from the statistical AFM analysis. (**A**) Representative wide-view AFM image of the exfoliated Sc-BPyDC (**2**). Thickness (**B**) and length (**C**) distribution histograms of the sample after the exfoliation. An arithmetic mean length, <L> of ~251 nm with an average thickness, <T> of ~53 nm is determined after measuring the dimensions of more than 100 individual nanosheets.

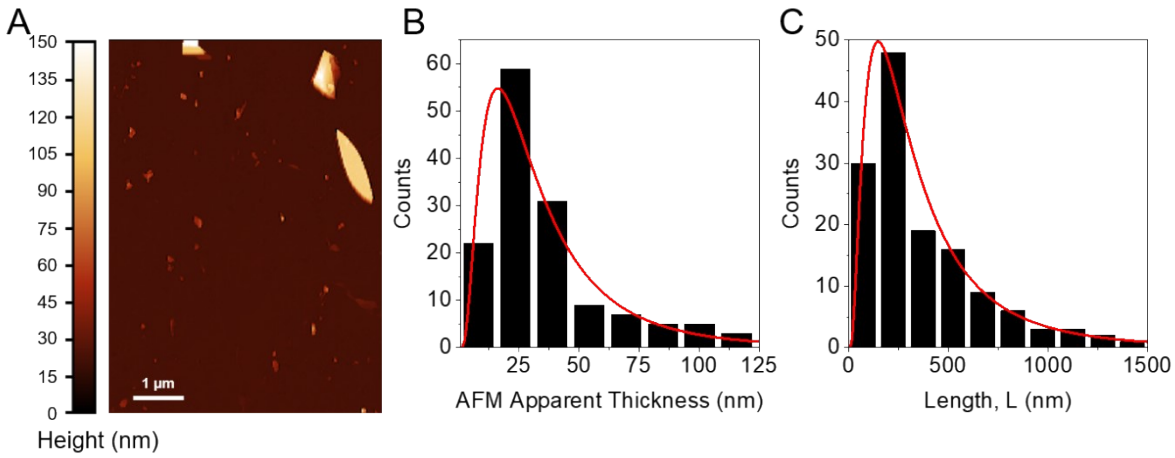

Figure S11: Raw data from the statistical AFM analysis. (**A**) Representative wide-view AFM image of the exfoliated Sc-CAU-11 (**3**). Thickness (**B**) and length (**C**) distribution histograms of the sample after the exfoliation. An arithmetic mean length, <L> of ~355 nm with an average thickness, <T> of ~36 nm is determined after measuring the dimensions of more than 100 individual nanosheets.

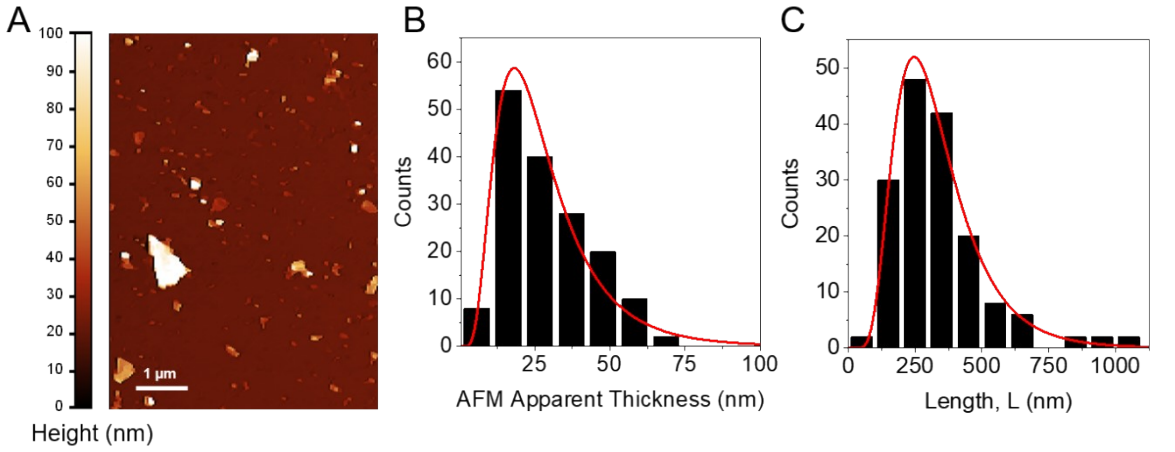

Figure S12: Raw data from the statistical AFM analysis. (**A**) Representative wide-view AFM image of the exfoliated Zr-FA-ODB (**4**). Thickness (**B**) and length (**C**) distribution histograms of the sample after the exfoliation. An arithmetic mean length, <L> of ~288 nm with an average thickness, <T> of ~28 nm is determined after measuring the dimensions of more than 100 individual nanosheets.

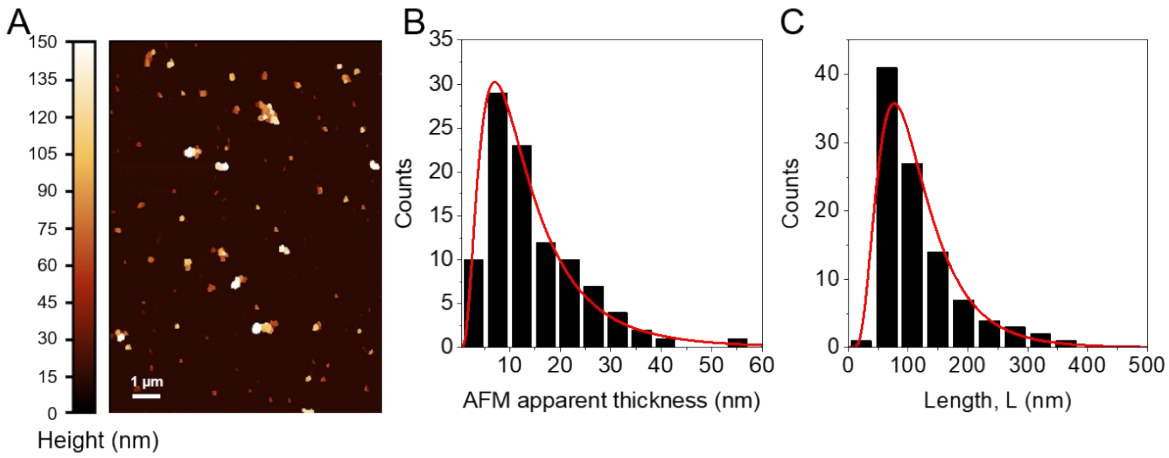

Figure S13: Raw data from the statistical AFM analysis. (**A**) Representative wide-view AFM image of the exfoliated Zr-CAU-39 (**5**). Thickness (**B**) and length (**C**) distribution histograms of the sample after the exfoliation. An arithmetic mean length, <L> of ~88 nm with an average thickness, <T> of ~14 nm is determined after measuring the dimensions of more than 100 individual nanosheets.

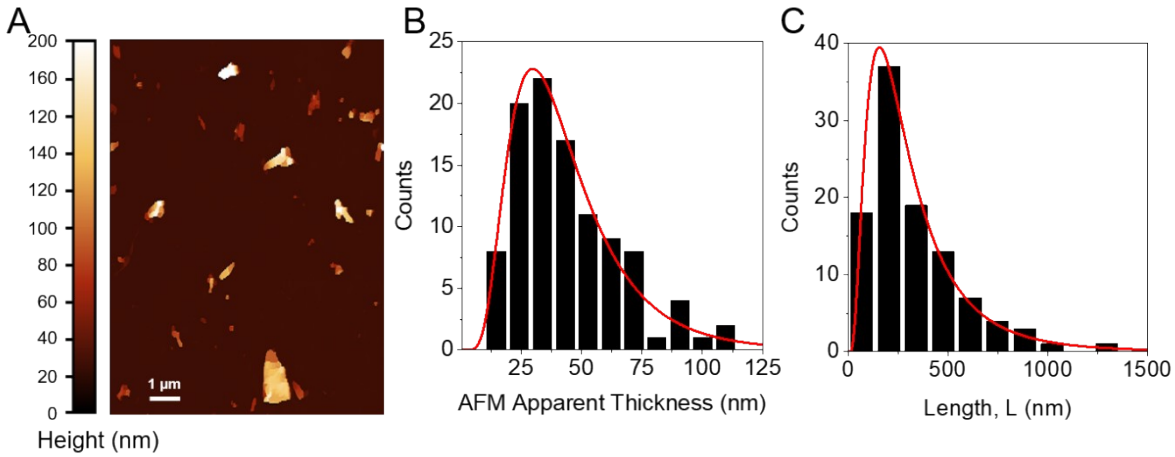

Figure S14: Raw data from the statistical AFM analysis. (**A**) Representative wide-view AFM image of the exfoliated Zr-CAU-45 (**6**). Thickness (**B**) and length (**C**) distribution histograms of the sample after the exfoliation. An arithmetic mean length, <L> of ~286 nm with an average thickness, <T> of ~43 nm is determined after measuring the dimensions of more than 100 individual nanosheets.

Bar charts from statistical AFM analysis

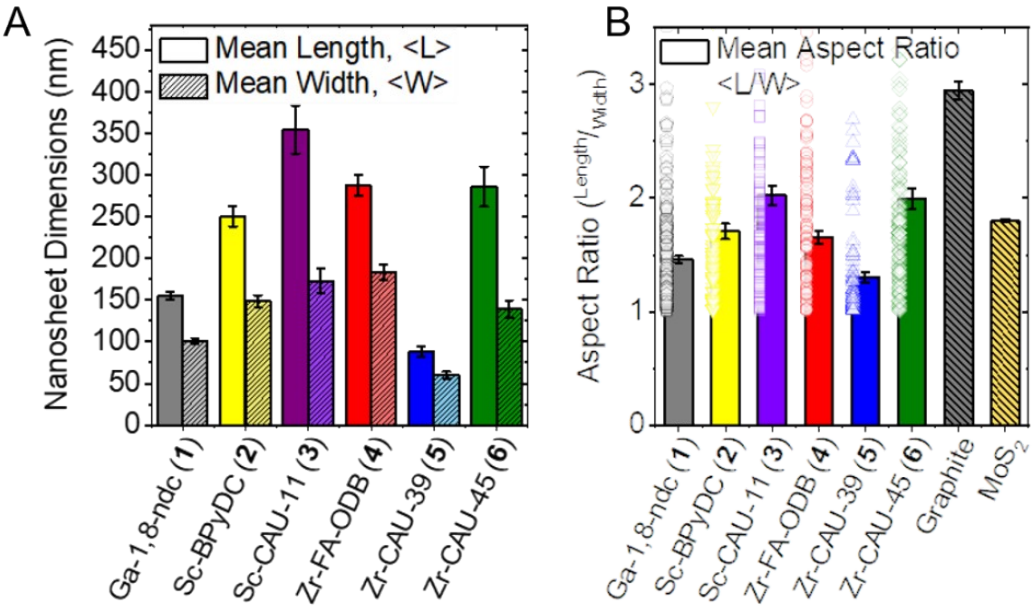

Figure S15: Bar charts of 2D MOF nanosheet dimensions. Mean nanosheet length and width (**A**) as determined from statistical evaluation of the nanosheet dispersions. The average length/width aspect ratio is shown in comparison to exfoliated graphite and MoS_2, as reported previously (**B**).[17]

5. Interlayer interactions in Sc-CAU-11

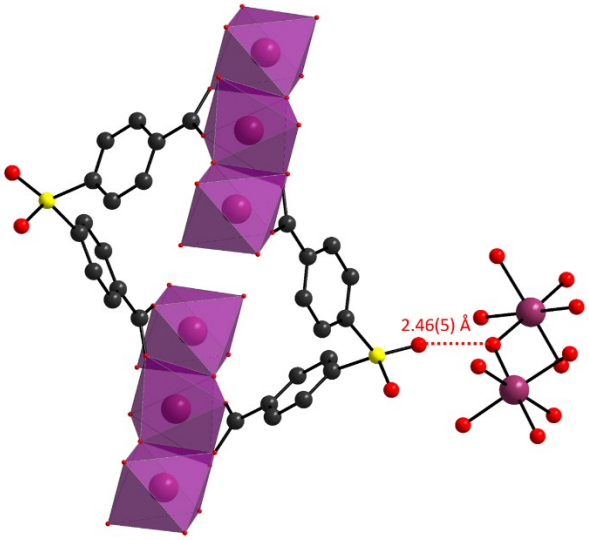

Figure S16: Structure of Sc-CAU-11 (**3**). A hydrogen bond (2.46(5) Å) is located between the sulfone group of the linker molecule and the bridging hydroxyl group of the inorganic building unit.[4]

6. Extended discussion on factors controlling nanosheet morphology

As mentioned in the main manuscript, many factors can be thought of to play a crucial role in LPE of layered compounds. In the following, we aim to discuss these. Unfortunately, a fully comprehensive understanding is lacking and available data in literature is based on rather random sampling. Therefore, it might not be possible to translate all findings across all materials.

A) Impact of the morphology of the starting material

While it was suggested by Savjani *et al.*[18] that the morphology of MoS_2 crystals subjected to sonication-assisted LPE has an impact on the morphology (e.g. area/thickness aspect ratio), this initial finding could not ultimately be confirmed. For example, Ott *et al.*[19] showed that the aspect ratio of MoS_2 nanosheets was independent of the morphology of the starting material across six commercially available MoS_2 bulk materials. For relatively long sonication times of 5h, not even the yield was significantly affected. It was however found that the optical response *(e.g.* photoluminescence intensity of monolayers) was affected suggesting that that nanosheet from different starting materials vary in defectiveness.

B) Impact of exfoliation conditions

While many methods exist to supply the energy required for exfoliation in LPE,[20-22] it is currently not clear whether these have an impact on the area/thickness aspect ratios of the obtained sheets. More frequently yield is assessed. [21, 23, 24] Literature data is often not comparable and typically involves different post-treatment conditions (such as centrifugation) in combination with a non-standardized analysis across research laboratories. Overall, a correlation of area and thickness of (few-layered) graphene nanosheets was observed across different institutions.[17, 25, 26] This suggests a well-defined aspect ratio of area and thickness as analyzed in detail in ref.[17, 27] While the kinetics of the exfoliation should not be neglected, [7, 15] it appears that a similar picture is obtained across laboratories and exfoliation methods in terms of aspect ratios. Unfortunately, we are not aware of a direct comparison, but our own data suggests that the exfoliation method (tip *versus* bath sonication) only has a minor impact on the obtained area/thickness aspect ratio, as shown for graphite in [17]. While this is surely currently a matter of debate, we note that exfoliation conditions (bath sonication, concentration, post treatment) was maintained identical in this study so that results are comparable.

C) Stabilizer in LPE

Since we used aqueous surfactant in this work, we focus on this aspect of nanosheet stabilization. While Griffin *et al.*[28] showed that the concentration of the (charged) surfactant has an impact on the yield, lateral size and thickness of the nanomaterial (graphene, WS_2 and MoS_2), the choice of surfactant and indeed surfactant concentration had no significant impact on the length/thickness aspect ratio of the nanosheets when employing "traditional" surfactants such as the one used here. However, we note that recent work by Read *et al.*[26] did show that the area/thickness aspect ratio can be different when using surfactants with binding schemes beyond purely van der Waals interaction between surfactant and solute. This tempted us to suggest the nature of the linker might have an impact of ease of exfoliation.

7. Calculation of the edge to surface energy ratio E_E/E_S

Using length/thickness aspect ratios to compare ease of exfoliation can be associated with a number of problems. For example, different materials might intrinsically possess different nominal thicknesses of one layer based on their crystal structure. In addition, the measured, apparent AFM thickness from LPE sheets is typically larger than the thickness of one layer due to adsorbed or intercalated solvent. Even in the case of micromechanically exfoliated graphene, the measured thickness depends on scanning conditions and the surface chemistry of the sample (in ambient conditions).[29] While this can be mitigated using adequate imaging modes,[30] the issue with intercalated and adsorbed solvent remains.

To this end, we and others have established "step height analysis", i.e. the measurement of the AFM height of >50 terraces on the surface of incompletely exfoliated nanosheets. The obtained apparent thicknesses of the terrace height will come as package of discrete steps which represent a multiple of the apparent height of a single layer. For many common materials with well resolved steps and terraces, this is a tedious, but feasible approach. However, it becomes increasingly challenging for nanosheets with lower length/thickness aspect ratio. For the thickness values reported in the main manuscript, the apparent AFM thickness is displayed, since step height analysis was beyond the scope of this manuscript.

To nonetheless be able to assess the ease of exfoliation in a comparative manner, we first analyzed the empirical nanosheet step height (h_{AFM}) of other materials reported in literature to test whether a scaling with the actual crystallographic thickness is observed. The materials, their crystallographic materials, their step height and a reference to the data is summarized in Table S3.

Table S3: Crystallographic thickness, h_0 and empirical AFM height of LPE nanosheets produced from different bulk crystals reported in literature.

Material	**h_0 [nm]**	**AFM step height [nm]**	**Reference**
Graphene	0.35	0.9	[24]
MoS_2	0.62	1.9	[31]
WS_2	0.63	1.9	[32]
GaS	0.75	1.5	[13]
h-BN	0.34	1.0	[33]
$Ni(OH)_2$	0.46	1.1	[34]
$NiPS_3$	0.66	1.5	[35]
Talc	0.94	2.1	[36]
MoO_2	0.63	0.9	[37]
GeTe	1.07	1.6	[38]
γ-InSe	0.54	1.5	[39]
$RuCl_3$	0.60	1.5	[39]
$CrTe_3$	1.10	1.9	[39]

In Figure S17, the step height is plotted as function of the crystallographic thickness (h_0) of one layer in the crystal. In spite of significant scatter, a roughly linear scaling is observed, suggesting that the step height can be estimated from the crystallographic thickness as $h_{AFM} = 2.24 \cdot h_0$. The data points are scattered within 25% deviation from the fitted line (grey background). The described relation between the crystallographic layer thickness and the AFM step height provides an important proxy for fast layer number estimation without tedious statistical analysis, in particular for materials where the step height is difficult to determine.

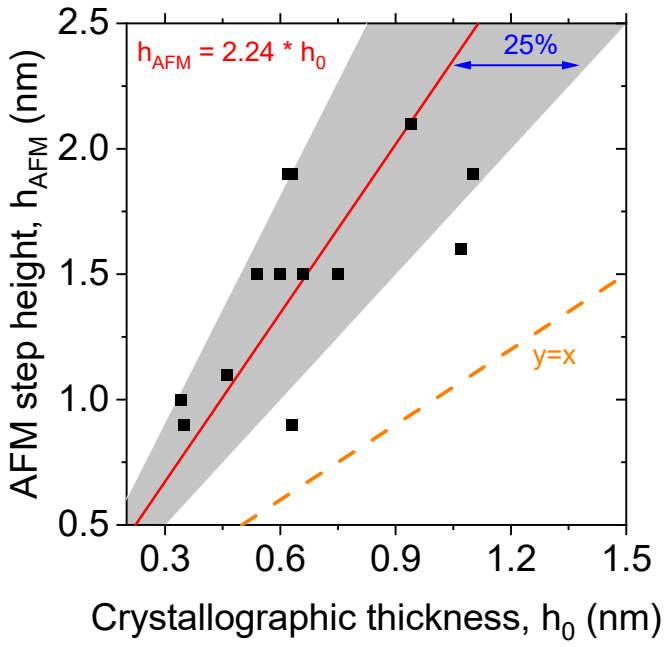

Figure S17: Empiric correlation between empirical AFM monolayer height (step height) and the crystallographic layer thickness across different materials. The observed trend can be used as proxy to avoid step height analysis for layer number estimation.

As described in detail elsewhere,[17] the energy ratio for creating new edges (E_E) to the energy required for peeling off a sheet per unit (E_S) is related to the average nanosheet dimensions expressed as area (<LW>) and layer number <N> according to the following equation:

$$< LW > = \left(2h_o \frac{E_E}{E_S}\right)^2 < N >^2 \quad (1)$$

Using the correlation between crystallographic thickness and the apparent thickness of one layer (step height), the measured thickness of a nanosheet can be expressed as

$$T = N * h_0 * 2.24 \quad (2)$$

with N being the layer number and h_0 the crystallographic thickness.

Combining equation (1) and (2) gives

$$\frac{\sqrt{\langle LW \rangle}}{\langle T/2.24 \cdot h_0 \rangle} = 2h_0 \frac{E_E}{E_S} \quad (3)$$

which allows to simplify the expression as

$$\langle T/2.24 \cdot h_0 \rangle = \frac{1}{n}\sum_i^n T_i/(2.24 \cdot h_0) = \frac{1}{2.24 \cdot n \cdot h_0}\sum_i^n T_i = \langle T \rangle/2.24 \cdot h_0 \quad (4)$$

to the following form:

$$\frac{\sqrt{\langle LW \rangle}}{0.893 \cdot \langle T \rangle} = \frac{E_E}{E_S} \quad (5)$$

Note that- due to the correlation between apparent monolayer height and crystallographic thickness established above- h_0 cancels out from the equation which means that it is not required to know the crystallographic thickness to compare ease of exfoliation across different materials. This also means that the measured length/thickness aspect ratio from AFM is indeed a more robust indicator for ease of exfoliation than one would expect if we assume that the ease of exfoliation is predominantly governed by the ratio of in-plane to out-of-plane binding strength. Of course, this is only the case if the correlation between crystallographic thickness and AFM step height was validated further which is beyond the scope of this work.

In the main manuscript, we have chosen to display the experimental edge to surface energy ratios along with the area/thickness aspect ratio to make it clear to a non-specialized reader that we have indeed considered that the different structures have different crystallographic thicknesses. To do this, the square root of the arithmetic mean nanosheet area per nanosheet thickness was calculated (Figure 2H in the main manuscript) and divided by 0.893 to determine the edge to surface energy ratio, E_E/E_S, where E_E is the energy required to create edges (i.e. tearing) and E_S the energy required for peeling off a sheet per unit area (i.e. delamination). Note that we aware that this is all based on a relatively minimal exfoliation model in combination with empirical data. Future work will be required for a more comprehensive picture.

8. References

1. L. Ueberricke, J. N. Coleman and C. Backes, *Phys. Status Solidi B*, 2017, **254**, 1700443.
2. T. Rabe, H. Pewe, H. Reinsch, T. Willhammar, E. Svensson Grape and N. Stock, *Dalton Transactions*, 2020, **49**, 4861-4868.
3. P. Rönfeldt, N. Ruser, H. Reinsch, E. S. Grape, A. Ken Inge, M. Suta, H. Terraschke and N. Stock, *Eur. J. Inorg. Chem.*, 2020, **2020**, 2737-2743.
4. P. Rönfeldt, H. Reinsch, N. Faßheber, H. Terraschke and N. Stock, *Eur. J. Inorg. Chem.*, 2020, **2020**, 1147-1152.
5. S. Waitschat, H. Reinsch, M. Arpacioglu and N. Stock, *Cryst. Eng. Comm.*, 2018, **20**, 5108-5111.
6. S. Leubner, V. E. G. Bengtsson, K. Synnatschke, J. Gosch, A. Koch, H. Reinsch, H. Xu, C. Backes, X. Zou and N. Stock, *J. Am. Chem. Soc.*, 2020, **142**, 15995-16000.
7. J. Texter, *Angew. Ch. Int. Ed.*, 2015, **54**, 10258-10262.
8. Z. Li, R. J. Young, C. Backes, W. Zhao, X. Zhang, A. Zhukov, E. Tillotson, A. P. Conlan, F. Ding, S. J. Haigh, K. S. Novoselov and J. N. Coleman, *ACS Nano*, 2020, **14**, 10976–10985.
9. J. N. Coleman, *Acc. Chem. Res.*, 2013, **46**, 14-22.
10. U. Khan, A. O'Neill, M. Lotya, S. De and J. N. Coleman, *Small*, 2010, **6**, 864-871.
11. A. O'Neill, U. Khan and J. N. Coleman, *Chem. Mater.*, 2012, **24**, 2414-2421.
12. D. Hanlon, C. Backes, T. M. Higgins, M. Hughes, A. O'Neill, P. King, N. McEvoy, G. S. Duesberg, B. Mendoza Sanchez, H. Pettersson, V. Nicolosi and J. N. Coleman, *Chem. Mater.*, 2014, **26**, 1751-1763.
13. A. Harvey, C. Backes, Z. Gholamvand, D. Hanlon, D. McAteer, H. C. Nerl, E. McGuire, A. Seral-Ascaso, Q. M. Ramasse, N. McEvoy, S. Winters, N. C. Berner, D. McCloskey, J. Donegan, G. Duesberg, V. Nicolosi and J. N. Coleman, *Chem. Mater.*, 2015, **27**, 3483–3493.
14. D. Hanlon, C. Backes, E. Doherty, C. S. Cucinotta, N. C. Berner, C. Boland, K. Lee, P. Lynch, Z. Gholamvand, A. Harvey, S. Zhang, K. Wang, G. Moynihan, A. Pokle, Q. M. Ramasse, N. McEvoy, W. J. Blau, J. Wang, G. Abellan, F. Hauke, A. Hirsch, S. Sanvito, D. D. O'Regan, G. S. Duesberg, V. Nicolosi and J. N. Coleman, *Nat. Commun.*, 2015, **6**, 8563.
15. H. Tao, Y. Zhang, Y. Gao, Z. Sun, C. Yan and J. Texter, *Phys. Chem. Chem. Phys.*, 2017, **19**, 921-960.
16. C.-X. Hu, Y. Shin, O. Read and C. Casiraghi, *Nanoscale*, 2021, **13**, 460-484.
17. C. Backes, D. Campi, B. M. Szydlowska, K. Synnatschke, E. Ojala, F. Rashvand, A. Harvey, A. Griffin, Z. Sofer, N. Marzari, J. N. Coleman and D. D. O'Regan, *ACS Nano*, 2019, **13**, 7050-7061.
18. N. Savjani, E. A. Lewis, R. A. D. Pattrick, S. J. Haigh and P. O'Brien, *RSC Adv.*, 2014, **4**, 35609-35613.
19. S. Ott, N. Wolff, F. Rashvand, V. J. Rao, J. Zaumseil and C. Backes, *Chem. Mater.*, 2019, **31**, 8424-8431.
20. M. Yi and Z. Shen, *J. Mater. Chem. A*, 2015, **3**, 11700-11715.
21. P. G. Karagiannidis, S. A. Hodge, L. Lombardi, F. Tomarchio, N. Decorde, S. Milana, I. Goykhman, Y. Su, S. V. Mesite, D. N. Johnstone, R. K. Leary, P. A. Midgley, N. M. Pugno, F. Torrisi and A. C. Ferrari, *ACS Nano*, 2017, **11**, 2742–2755.
22. K. R. Paton, J. Anderson, A. J. Pollard and T. Sainsbury, *Mater. Res. Exp.*, 2017, **4**, 025604.
23. P. Turner, M. Hodnett, R. Dorey and J. D. Carey, *Sci. Rep.*, 2019, **9**, 8710.
24. K. R. Paton, E. Varrla, C. Backes, R. J. Smith, U. Khan, A. O'Neill, C. Boland, M. Lotya, O. M. Istrate, P. King, T. Higgins, S. Barwich, P. May, P. Puczkarski, I. Ahmed, M. Moebius, H. Pettersson, E. Long, J. Coelho, S. E. O'Brien, E. K. McGuire, B. M. Sanchez, G. S. Duesberg, N. McEvoy, T. J. Pennycook, C. Downing, A. Crossley, V. Nicolosi and J. N. Coleman, *Nat. Mater.*, 2014, **13**, 624-630.
25. T. F. D. Fernandes, D. R. Miquita, E. M. Soares, A. P. Santos, L. G. Cançado and B. R. A. Neves, *2D Mater.*, 2020, **7**, 025045.
26. O. Read, Y. Shin, C.-x. Hu, M. Zarattini, M. Boyes, X. Just-Baringo, A. Panigrahi, I. Larrosa and C. Casiraghi, *Carbon*, 2022, **186**, 550-559.

27. L.-J. Ji, Y. Qin, D. Gui, W. Li, Y. Li, X. Li and P. Lu, *Chem. Mater.*, 2018, **30**, 8732-8738.
28. A. Griffin, K. Nisi, J. Pepper, A. Harvey, B. M. Szydłowska, J. N. Coleman and C. Backes, *Chem. Mater.*, 2020, **32**, 2852-2862.
29. P. Nemes-Incze, Z. Osváth, K. Kamarás and L. P. Biró, *Carbon*, 2008, **46**, 1435-1442.
30. C. J. Shearer, A. D. Slattery, A. J. Stapleton, J. G. Shapter and C. T. Gibson, *Nanotechn.*, 2016, **27**, 125704.
31. C. Backes, R. J. Smith, N. McEvoy, N. C. Berner, D. McCloskey, H. C. Nerl, A. O'Neill, P. J. King, T. Higgins, D. Hanlon, N. Scheuschner, J. Maultzsch, L. Houben, G. S. Duesberg, J. F. Donegan, V. Nicolosi and J. N. Coleman, *Nat. Commun.*, 2014, **5**, 4576.
32. C. Backes, B. M. Szydłowska, A. Harvey, S. Yuan, V. Vega-Mayoral, B. R. Davies, P.-l. Zhao, D. Hanlon, E. J. G. Santos, M. I. Katsnelson, W. J. Blau, C. Gadermaier and J. N. Coleman, *ACS Nano*, 2016, **10** 1589-1601.
33. A. Griffin, A. Harvey, B. Cunningham, D. Scullion, T. Tian, C.-J. Shih, M. Gruening, J. F. Donegan, E. J. G. Santos, C. Backes and J. N. Coleman, *Chem. Mater.*, 2018, **30**, 1998-2005.
34. A. Harvey, X. He, I. J. Godwin, C. Backes, D. McAteer, N. C. Berner, N. McEvoy, A. Ferguson, A. Shmeliov, M. E. G. Lyons, V. Nicolosi, G. S. Duesberg, J. F. Donegan and J. N. Coleman, *J. Mater. Chem. A*, 2016, **4**, 11046-11059.
35. K. Synnatschke, S. Shao, J. van Dinter, Y. J. Hofstetter, D. J. Kelly, S. Grieger, S. J. Haigh, Y. Vaynzof, W. Bensch and C. Backes, *Chem. Mater.*, 2019, **31**, 9127–9139.
36. H. Andrew, B. B. John, G. Ian, G. K. Adam, M. S. Beata, M. Ghulam, T. Andrew, J. L. David, O. B. Paul and N. C. Jonathan, *2D Mater.*, 2017, **4**, 025054.
37. J. B. Boland, A. Harvey, R. Tian, D. Hanlon, V. Vega-Mayoral, B. M. Szydłowska, A. Griffin, T. Stimpel-Lindner, S. Metel, V. Nicolosi, G. Duesberg and J. N. Coleman, *Nanoscale Advances*, 2019, **1**, 1560-1570.
38. P. Zhang, F. Zhao, P. Long, Y. Wang, Y. Yue, X. Liu, Y. Feng, R. Li, W. Hu, Y. Li and W. Feng, *Nanoscale*, 2018, **10**, 15989-15997.
39. K. Synnatschke, *Dissertation: Liquid Phase Exfoliation and Size-dependent Properties of van der Waals Crystals*, Combined Faculty of Natural Sciences and Mathematics Heidelberg University, 2021.